

Silicon nanowire-based ring-shaped tri-axial force sensor for smart integration on guidewire

This content has been downloaded from IOPscience. Please scroll down to see the full text.

2014 J. Micromech. Microeng. 24 065002

(<http://iopscience.iop.org/0960-1317/24/6/065002>)

View [the table of contents for this issue](#), or go to the [journal homepage](#) for more

Download details:

IP Address: 117.17.182.69

This content was downloaded on 01/05/2014 at 06:01

Please note that [terms and conditions apply](#).

Silicon nanowire-based ring-shaped tri-axial force sensor for smart integration on guidewire

Beibei Han^{1,2}, Yong-Jin Yoon², Muhammad Hamidullah¹,
Angel Tsu-Hui Lin¹ and Woo-Tae Park³

¹ Institute of Microelectronics (IME), A*STAR (Agency for Science, Technology and Research),
11 Science Park Road, 117685, Singapore

² School of Mechanical and Aerospace Engineering, Nanyang Technological University,
50 Nanyang Avenue, 639798, Singapore

³ Department of Mechanical and Automotive Engineering, Seoul National University of Science and
Technology, Seoul, Korea

E-mail: yongjiny@ntu.edu.sg and wtpark@seoultech.ac.kr

Received 3 February 2014

Accepted for publication 21 February 2014

Published 25 April 2014

Abstract

A ring-shaped tri-axial force sensor with a $200\ \mu\text{m} \times 200\ \mu\text{m}$ sensor area using silicon nanowires (SiNWs) as piezoresistive sensing elements is developed and characterized. The sensor comprises a suspended ring structure located at the center of four suspended beams that can be integrated on the distal tip of a guidewire by passing through the hollow core of the sensor. SiNWs with a length of $6\ \mu\text{m}$ and a cross section of $90\ \text{nm} \times 90\ \text{nm}$ are embedded at the anchor of each silicon bridge along $\langle 110 \rangle$ direction as the piezoresistive sensing element. Finite element analysis has been used to determine the location of maximum stress and the simulation results are verified with the experimental measurements. Taking advantage of the high sensitivity of SiNWs, the fabricated ring-shaped sensor is capable of detecting small displacement in nanometer ranges with a sensitivity of $13.4 \times 10^{-3}\ \mu\text{m}^{-1}$ in the z -direction. This tri-axial force sensor also shows high linearity ($>99.9\%$) to the applied load and no obvious hysteresis is observed. The developed SiNW-based tri-axial force sensor provides new opportunities to implement sensing capability on medical instruments such as guidewires and robotic surgical grippers, where ultra-miniaturization and high sensitivity are essential.

Keywords: silicon nanowire, tri-axial force sensor, minimally invasive surgery, guidewire

(Some figures may appear in colour only in the online journal)

1. Introduction

The trend towards minimally invasive medical procedures is driving the development of ultra-miniaturized sensors that are highly sensitive and physically robust. Minimally invasive-based catheterization procedures, such as cardiovascular and thoracic interventional procedures, are becoming increasingly popular in medical practice for both diagnosis and surgery [1]. In these procedures, medical instruments such as catheters and guidewires are inserted into the patient, passing through blood vessels to treat tissues and organs. Comparing with traditional

open surgery, these minimally invasive procedures have numerous advantages, as reported in [2]. However, because the medical instruments such as catheters and guidewires are controlled outside of the patient's body, limitations such as the total loss of force sensation, insufficient vision information from 2D images [3], and exposure of patients and surgeons to radiation during x-ray fluoroscopy, make the procedure challenging and require a certain level of operational skills from surgeons, especially in the cases of stenosed lesions and complex blood vessels, as illustrated in figure 1.

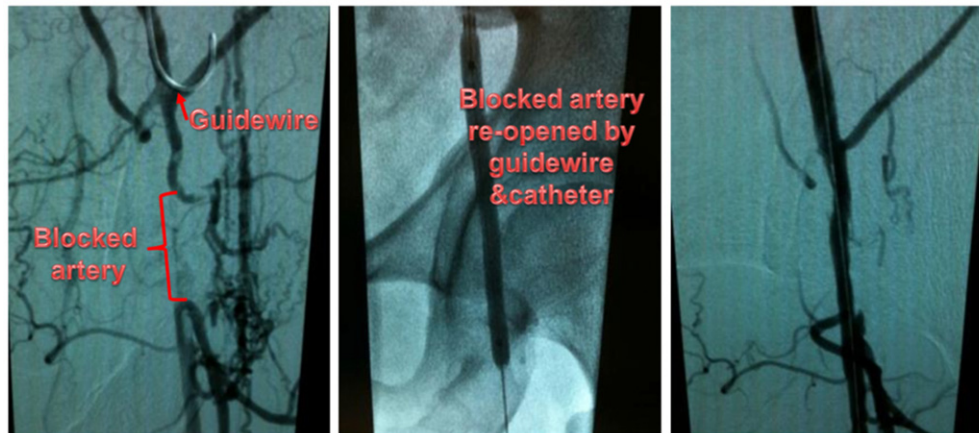


Figure 1. Screen shot captured from an angiogram during surgery. The guidewire passes through the lesion and the balloon catheter opens up the blocked artery to allow the artery to re-open (pictures from the National University Hospital of Singapore).

To increase the manipulation safety and accuracy of catheters and guidewires inside blood vessels, several techniques have been proposed. The magnetic resonance imaging (MRI) technique has been widely used to guide the catheter and guidewire insertion [4]. It can provide high quality 3D images without harmful radiation. Intravascular ultrasound (IVUS) devices are also becoming popular nowadays as they can offer high-resolution anatomical images of the blood vessel from inside the body [5, 6]. Despite the aforementioned advantages, both MRI and IVUS techniques are insufficient to provide detailed force information about the interaction between the tip of the catheter or guidewire and the blood vessels. Recent studies have shown that the contact force is a determinant factor for determining lesion size during catheterization procedures [7–9]. Therefore, the development of catheters and guidewires with force sensing capabilities by integrating force sensors at their tips has become of great interest.

Many types of miniaturized sensors have been developed and integrated on the tips of catheters and guidewires [8, 10–19]. The ultra-miniaturization and sensitivity requirements for sensors to be integrated on guidewires are challenging as the tip diameter of a typical guidewire is only 0.36 mm, which is among the smallest instruments inserted into the human body. A number of studies have reported good results on sensor miniaturization and have demonstrated the successful integration of sensors on a guidewire. For example, E Kalvesten *et al* [14] reported the integration of a miniaturized sensor on a guidewire for balloon angioplasty application. In this work, a surface micromachined piezoresistive pressure sensor was mounted in a recess near the tip of a guidewire with an outer diameter of 0.36 mm, from the work of which a commercialized guidewire named Pressure-Wire was produced by St Jude Medical Systems [20]. As another example, T Meiß *et al* [16] reported a MEMS force sensor integrated on a 360 μm diameter guidewire to measure contact forces during angioplasty. The sensor was encapsulated at the tip of guidewire with an elastomer and had a force resolution of 1 mN. However, quite a few of the developed sensors turned out to be complex and difficult to integrate on guidewires and

some of them have changed the standard manufacturing flow of guidewires to fit in with the sensor designs.

In this paper, we report a novel ring-shaped tri-axial force sensor for easy integration with guidewires. With the ring-shaped structure design, the sensor can be easily mounted on the circular core wire at the tip of a guidewire. Together with the movable core wire, the sensor can detect three axis forces while maintaining the original welded tip, which is an essential part of the standard guidewire assembly.

Regarding to the tri-axial force sensors, a considerable amount of research has been conducted on developing tri-axial force sensors to detect both normal and shear forces in robotics and biomedical applications [21–29]. Table 1 summarizes the recently reported tri-axial force sensor designs. Kane *et al* [22] proposed a polysilicon-based piezoresistive complementary metal-oxide semiconductor (CMOS)-compatible tactile sensor for grasping applications in robotic manipulators, where poly piezoresistors are embedded in the four bridges as sensing elements. A sensitivity of 1.59 mV kPa⁻¹ in normal direction and 0.32 mV kPa⁻¹ in shear direction was reported. However, due to the flat shuttle plate design without an additional shear force enhancing mechanism, the shear sensitivity was reported to be five times lower than the normal sensitivity. To increase the shear force sensitivity, force sensors with various types of structural design have been developed, including diaphragm-type sensor designs with an additional mesa acting as a shear force transferring element [23–26, 28] and biomimetic tactile sensors designs with epidermal ridges [29]. Nevertheless, most of the previously reported tri-axial force sensors are designed for robotics and biomedical applications and cannot be directly adapted for catheterization applications due to their incompatible mechanical structure designs, as well as their bulk dimensions.

Recent research on nanoscale transduction mechanisms such as silicon nanowires (SiNWs) and carbon nanotubes have provided a great opportunity to significantly reduce the size of MEMS devices for biomedical applications where ultra-miniaturization is essential, such as guidewire applications. Compared to conventional metal strain gauges and bulk implanted piezoresistors, the outstanding piezoresistive performance of single crystal SiNWs has been reported by

Table 1. Summary of recently reported tri-axial force sensor designs together with the ring-shaped design.

Shear force transfer method	Application	Sensing element	Size (μm)	Sensitivity	Linearity	Force range	References
Guidewire or micro pillar	Guidewire navigation	Silicon nanowire	$380 \times 380 \times 10$	$S_{Dz} = 13.4 \times 10^{-3} \mu\text{m}^{-1}$ $S_{Fz} = 0.734 \text{ N}^{-1}$	0.999	20 mN	This work
Fabricated silicon rod	Minimally invasive surgery	Polysilicon piezoresistor	Diaphragm: $420 \times 420 \times 7$ Post:H 470 μm	$S_{Dz} = 6.0 \times 10^{-3} \mu\text{m}^{-1}$ $S_{Dx} = 1.2 \times 10^{-3} \mu\text{m}^{-1}$ $S_{Fz} = 3.5 \text{ N}^{-1}$ $S_{Fx} = 10.8 \text{ N}^{-1}$	n.a.	0–0.05 N	Hu <i>et al</i> 2010 [28]
Added epoxy mesa	Robotic control	Boron implanted p+ piezoresistor	$300 \times 300 \times 45$	4–6 mV/mN/V	n.a.	0–3 mN	Vasarhelyi <i>et al</i> 2006 [27]
Silicon mesa fabricated on the sensor	Amputees prosthesis	Boron implanted p+ piezoresistor	$2.3 \text{ mm} \times 2.3 \text{ mm} \times 1.33 \text{ mm}$	$S_z = 0.032 \pm 0.001 \text{ N}^{-1}$ $S_x = S_y = 0.0323 \text{ N}^{-1}$	0.997	0–2 N	Beccai <i>et al</i> 2005 [25]
Planar structure	Grasping in robotic manipulator	Polysilicon piezoresistor	Array: $19.2 \text{ mm} \times 19.2 \text{ mm}$	$S_z = 1.59 \text{ mV kPa}^{-1}$ $S_x = S_y = 0.32 \text{ mV kPa}^{-1}$	0.999	Normal: 0.35 mN ^a Shear: 0.6 mN ^a	Kane <i>et al</i> 2000 [22]
Attached SU8 square mesa	Hand grasping activity	Boron implanted p+ piezoresistor	Diaphragm: $1.9 \text{ mm} \times 1.9 \text{ mm} \times 50$ Mesa: H 60	$S_z = 1.57 \text{ N}^{-1}$ S_x, S_y varies with loading conditions	0.98	0–3 N	Wang and Beebe 2000 [23] Bütefisch <i>et al</i>
Stylus attached by epoxy resin	Material characterization	Piezoresistor	$5 \text{ mm} \times 5 \text{ mm} \times 0.36 \text{ mm}$	$S_z = 0.36 \text{ N}^{-1}$ $S_x = S_y = 13.2 \text{ N}^{-1}$	n.a.	n.a.	2001 [24]

^a Unit converted from normal force range of 35 kPa and shear force range of 60 kPa to mili Newton in order to be identical to other designs.

many research groups [30–35] and the scalability of the SiNW-based device has been successfully demonstrated in many MEMS device designs [36–39]. Therefore, in this paper, a force sensor utilizing a SiNW as the piezoresistive sensing element is developed. There are many reported methods for the integration of nanomaterials onto MEMS devices to utilize sensing functionality. The SiNWs can be either fabricated using the bottom-up approach and then transferred onto the pre-fabricated MEMS device [40], or they can be fabricated by using the top-down technique directionally along with the MEMS device fabrication [41]. In this paper, SiNWs with a cross section of $90 \text{ nm} \times 90 \text{ nm}$ were fabricated by using the top-down approach using lithographic pattern transfer and thermal dry oxidation processes. Taking advantage of the high sensitivity of SiNWs, the fabricated ring-shaped sensor is capable of detecting small displacement in nanometer ranges with a sensitivity of $13.4 \times 10^{-3} \mu\text{m}^{-1}$ along the z -direction.

2. Force sensor design

2.1. Sensor design

The ring-shaped sensor design is inspired from the requirement of mounting a force sensor on the tip of a movable core guidewire. Meanwhile, the sensor could be adapted to a standard guidewire manufacturing process flow without changing the commercial guidewire structures. Generally, the structure of a guidewire comprises a distal tip, a central core wire, a coil, and an elastic cover. According to the structural design of the central core wire, commercial guidewires are mainly classified into two types: fixed core guidewire and movable core guidewire [42, 43], as shown in figure 2. The fixed core guidewire or 1-piece core guidewire shown in figure 2(a) has a tapered core wire that connects the weld distal tip and the proximal end. The movable core guidewire, which was introduced by Simpson *et al* in 1982

[44], has an independently movable, flexible-tipped core wire, as illustrated in figure 2(b). The moveable core guidewire is more flexible and steerable than the fixed core guidewire, and enables the reduction of trauma while traversing along blood vessels. In general, the tip of the standard movable guidewire is straight at the natural state and moveable in all directions. During insertion, the tip of the guidewire can be bent into different shape configurations under the outside control of surgeons. Compared to the fixed core configuration, the force sensation from the flexible tip of the moveable guidewire is hardly perceived. As shown in figure 2(c), a force sensor is designed to be integrated on the movable part of the core wire to measure the tip contact force between the guidewire and vessel walls. When external forces are applied at the distal tip of the guidewire, displacement differences between the distal tip and the coil will induce a deformation on the sensor structure. The sensor measures forces in both normal and shear directions, as shown in figure 2(d). An interface ASIC is integrated with the force sensor to read the force information applied on the sensor in the form of resistance and converts it to current pulse [45]. This ASIC interface also functions to reduce the number of input and output signal lines.

The force sensor consists of a suspended ring-shaped structure located at the center of four suspended cantilever beams with the axes perpendicular to each other, as shown in figure 3(a). Single crystal SiNWs are embedded at the end of each beam as the piezoresistive sensing element to leverage its high gauge factor. Compared with the previously reported tri-axial force sensor designs in [16, 18, 25], the ring shape sensor design is easy for sensor-guidewire assembly and adaptable to commercial guidewire structures. In addition, the assembly configuration of the ring-shaped sensor minimizes bending artifacts as it is directly integrated on the distal tip of the guidewire, whereas most of the previously reported sensors for catheterization applications were mounted in a recess near the tip of the core wire or on the wall of the catheter [14, 15, 20].

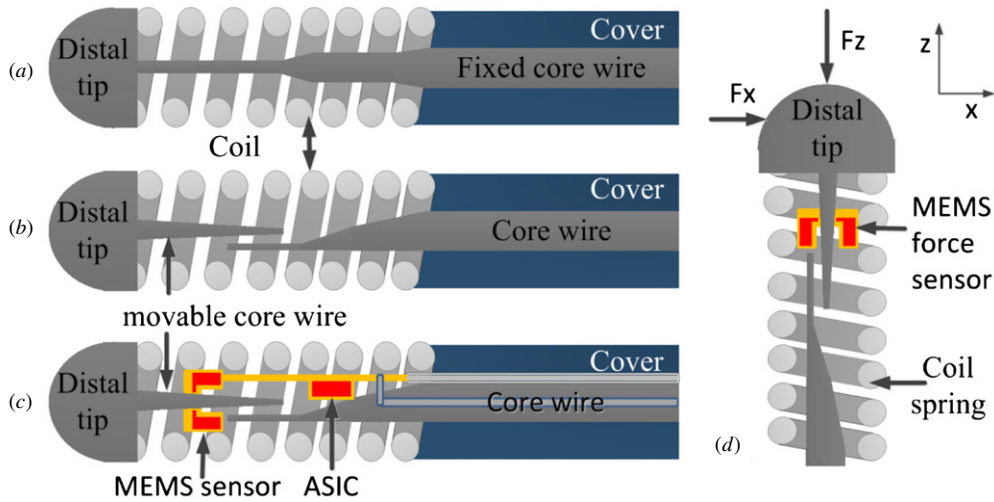
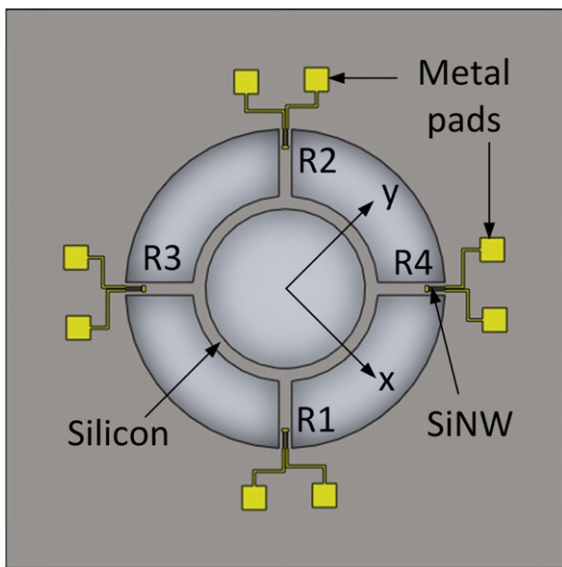
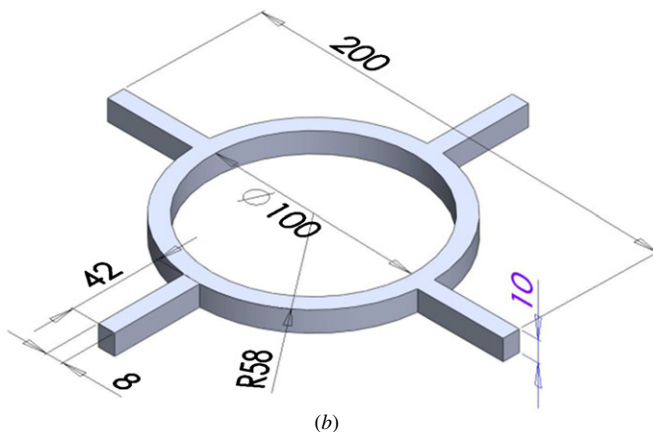


Figure 2. Illustration of the distal tip of the sensorized guidewire design: (a) standard fixed core guidewire, (b) standard movable core guidewire, (c) standard movable core guidewire with integrated MEMS force sensor and ASIC, (d) sensorized guidewire under forces applied at the distal tip.



(a)



(b)

Figure 3. (a) Schematic of the ring-shaped force sensor design. (b) Dimensions of the sensor structure: beam $42 \mu\text{m} \times 8 \mu\text{m} \times 10 \mu\text{m}$, inner ring diameter $100 \mu\text{m}$, and outer ring diameter $116 \mu\text{m}$.

Table 2. Material properties for the FEM modeling.

Material	Young's modulus	Poisson ratio	Density
Silicon	169 GPa	0.278	2330 kg m^{-3}
SiO_2	70 GPa	0.17	2200 kg m^{-3}
Steel	200 GPa	0.33	7850 kg m^{-3}
Epoxy	3.5 GPa	0.069	1250 kg m^{-3}

The dimension of the sensor can be determined according to the structural dimension of the guidewire, which is typically $360 \mu\text{m}$ at the tip. Considering restrictions such as the overall dimension of the designed sensor should not exceed the inner diameter of the coil and the diameter of the inner ring should be larger than the diameter of the movable core wire, the inner ring diameter was designed to be $100 \mu\text{m}$ and the diameter of the outer ring was designed to be $116 \mu\text{m}$. The cantilever beam has a size of $42 \mu\text{m} \times 8 \mu\text{m} \times 10 \mu\text{m}$ in length, width, and thickness, respectively, as shown in figure 3(b). The overall sensing area including the cantilever beams is $200 \mu\text{m} \times 200 \mu\text{m}$. A finite element analysis method was used to optimize the critical structural parameters of the sensor, such as the inner and outer diameters of the ring, and the cantilever length, width and thickness.

2.2. FEM modeling

A finite element analysis simulation tool, COMSOL, was used to study the mechanical behavior of the structure. The material properties used in the numerical analysis are shown in table 2 [46–48]. The ring was modeled as a double layer structure with a layer of $9 \mu\text{m}$ silicon and $1 \mu\text{m}$ silicon oxide (SiO_2) on top. In order to find the location with the maximum sensitivity to implement the piezoresistors, regions of highest stress on the beams were identified by finite element modeling (FEM), as shown in figure 4. When normal force is applied on the top surface of the ring, the sensor beams bend downward and the maximum stress is found at the bases of the beams. SiNWs are embedded between the layers of silicon and SiO_2 at these high

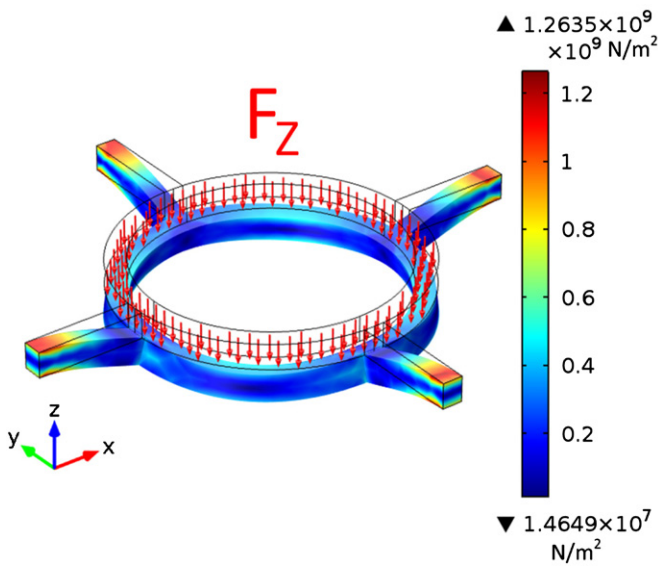


Figure 4. COMSOL modeling results of the ring structure under vertical load. The right color table shows the von Mises stress field of the sensor in response to 5 mN force applied in the z -direction. The maximum stress is found at the bases of the beams wherein the SiNWs are embedded.

stress regions in order to obtain the maximum piezoresistance output. To avoid the fracture of the structure, a value of 2.8 GPa

[49] was used as the silicon yield stress in the FEM analysis, and the maximum force that can be applied on the sensor was found to be 20 mN.

An FEM simulation of the designed ring-shaped sensor integrated with a steel wire is presented in figure 5, where the steel wire represents the distal tip of a movable core guidewire. For simplification, the function of the coil spring and the assembled distal tip of the guidewire were not considered in the simulation. As shown in figure 5(a), the steel wire passes through the ring and they are firmly attached by epoxy. In this case, the steel wire acts as force transferring element when shear load is applied. The stress field for normal and shear load is presented in figure 5(b). When a normal load is applied, the lateral stress components in the four SiNWs are equal in magnitude with same direction (figure 5(b) (left)). When a transverse loading is applied in the x - or y -direction, the two SiNWs along with the loading direction experience stress of the same magnitude with opposite signs while the other two SiNWs perpendicular to the loading undergo torsion (figure 5(b) (right)).

2.3. Force sensing principle

The relationship between the applied external force and the displacement on the SiNW ring-shaped sensor is

$$F = K_e \Delta x, \quad (1)$$

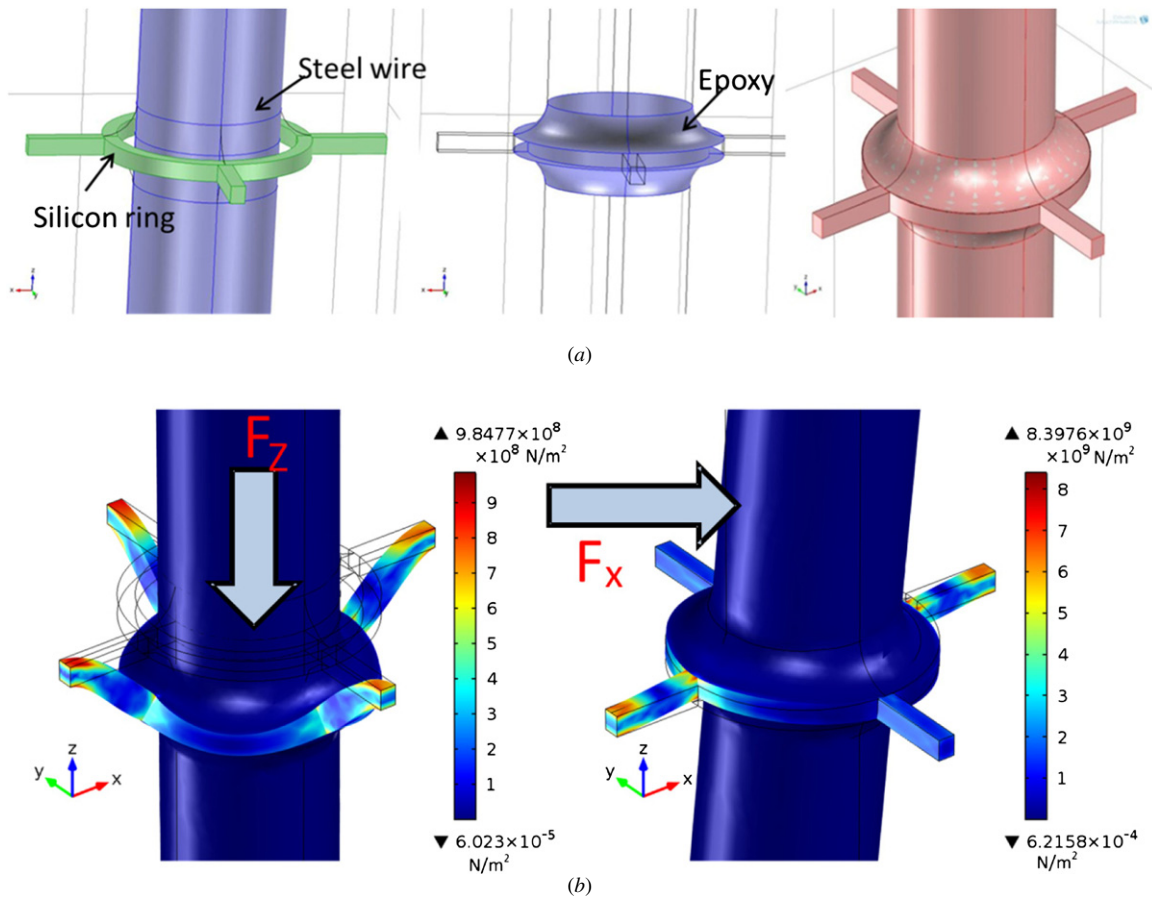


Figure 5. (a) Illustration of the ring sensor and steel wire integration by epoxy. (b) Sensor deformation under applied forces F_z (left) and F_x (right). The color table shows the von Mises stress field in response to 20 mN force applied in the z - and x -direction respectively.

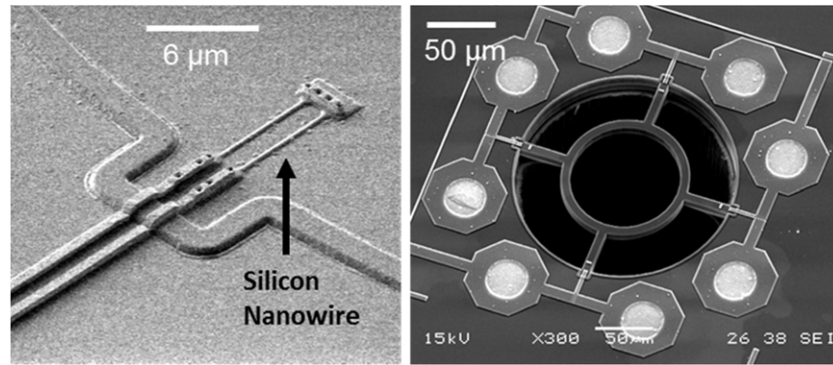


Figure 6. SEM image of the fabricated SiNW and the ring-shaped tactile sensor with four embedded SiNW piezoresistors.

where F is the applied force, K_e is the equivalent spring stiffness of the sensor structure, and Δx is the ring displacement.

The piezoresistors change their resistance due to beam deformation and induced strain. The resistance change is given by

$$\frac{\Delta R}{R} = \pi_l \sigma_l + \pi_t \sigma_t, \quad (2)$$

where R is the resistance without applied stress, ΔR is the resistance change with applied stress, π and σ represent the piezoresistive coefficient and stress respectively, and the subscripts l and t refer to longitudinal and transverse components [50].

The resistance change corresponding to the X - Y - Z direction are given by

$$\begin{aligned} S_x &= \left(\frac{\Delta R}{R} \right)_x = \frac{\Delta R_3}{R_3} - \frac{\Delta R_4}{R_4} \\ S_y &= \left(\frac{\Delta R}{R} \right)_y = \frac{\Delta R_1}{R_1} - \frac{\Delta R_2}{R_2} \\ S_z &= \left(\frac{\Delta R}{R} \right)_z = \frac{\Delta R_1}{R_1} + \frac{\Delta R_2}{R_2} + \frac{\Delta R_3}{R_3} + \frac{\Delta R_4}{R_4}. \end{aligned} \quad (3)$$

where R_1 , R_2 , R_3 , and R_4 are the resistance of each of the resistors as labeled in figure 3(a). When shear force is applied, the opposite piezoresistors such as R_1 and R_2 experience opposite strain (i.e., R_1 will experience tensile strain whereas R_2 will experience compressive strain, or vice versa). When normal loading is applied, the resistance of each of the four piezoresistors has the same sign of strain (either tensile or compressive). The Z axis sensitivity is defined as the total resistance change of the four piezoresistors.

3. Sensor fabrication

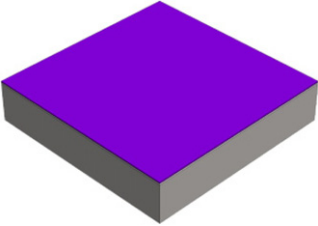

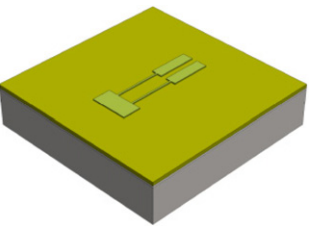
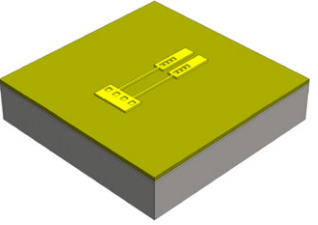
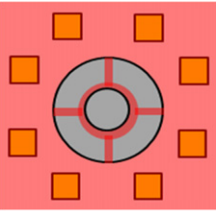
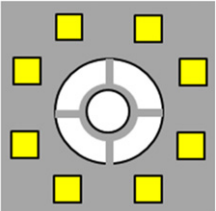






The force sensor fabrication involves two main steps, which are the SiNW fabrication and cantilever release. The critical fabrication steps are summarized in table 3.

The starting material was a (1 0 0)-oriented p-type silicon-on-insulator (SOI) wafer of a 117 nm thick top silicon layer on a 145 nm thick buried oxide (BOX) layer (table 3(a)). The top silicon layer was pre-doped with the resistivity of $13.5 \Omega \cdot \text{cm}$. The SiNWs were created by standard photolithography by using a Nikon KrF DUV lithography

scanner (model NSR-203B) along the $\langle 110 \rangle$ crystal orientation (table 3(b)). The mask critical dimension (CD) for the nanowires (NWs) was 160 nm. Once the silicon layer was patterned, the critical dimension of the NW line width was trimmed down to approximately 110 nm by etching the photoresist with a plasma-induced feeding gas ($\text{He}/\text{O}_2 + \text{N}_2$). After the silicon etching and resist removal process, a 2 h thermal oxidation process was carried out at 875°C to grow SiO_2 on the patterned SiNW. At the end of this step, SiNWs with an approximate length of $6 \mu\text{m}$ and a cross section of $90 \text{ nm} \times 90 \text{ nm}$ were achieved along the $\langle 110 \rangle$ crystal orientation. After that, p-type ion implantation was performed at the SiNW regions by BF_2^+ with a dosage of 1×10^{14} ions cm^{-2} and energy of 100 keV (tilt 7° and twist 22°). Then photolithography was performed to protect the SiNWs from the later highly doped implantation at the resistor connecting regions (paddle regions). A higher doped implantation with a dosage of 1×10^{15} ions cm^{-2} and an energy of 35 keV (tilt 7° and twist 0°) was performed at the three paddle regions for the low resistivity silicon trace and the silicon to metal contact. The three paddles, as indicated in table 3(c)–(e), were used to connect two nanowires and form an electrical signal path. Then the dopants were activated by rapid thermal annealing (RTA) at 1000°C for 30 s, and a $0.4 \mu\text{m}$ silicon oxide premetal dielectric was deposited (table 3(c)) followed by photolithography and silicon oxide etching for contact opening. After metal deposition, the metal was patterned by photolithography and metal etching. The process was continued by silicon oxide passivation and pads opening by photolithography and oxide etching (table 3(d)).

After the fabrication of SiNWs, the cantilevers and the ring of the sensor were released by using the deep reactive ion etching (DRIE) process. This fabrication process was started with patterning of a $2.5 \mu\text{m}$ photoresist sacrificial layer on the silicon oxide layer by standard photolithography, as shown in table 3(e). Next, silicon oxide was etched followed by a $10 \mu\text{m}$ silicon DRIE process. The thickness of the cantilever and the ring was defined as $10 \mu\text{m}$ at this step. After resist removal, a thin layer of silicon oxide was deposited by using a plasma-enhanced chemical vapor deposition (PECVD) process. The purpose of the PECVD process was to protect the sidewall from the silicon isotropic DRIE process during final cantilever release. After the PECVD process, the oxide was etched back

Table 3. Fabrication process flow.

Main fabrication flow	Process	Description
	(a) Wafer inspection	SOI wafer, 117 nm buried oxide (BOX) layer, 145 nm top silicon (device) layer lowly doped of boron (p-type) with resistivity of $13.5 \Omega \cdot \text{cm}$
	(b) SiNW pattern and thermal dry oxidation	Photolithography for SiNW patterning (160 nm) and resist trimming to 90 nm. Two hours thermal oxidation, followed by low doped implantation.
	(c) SiO ₂ PMD deposition	High doped implantation at paddle regions and 0.4 μm silicon oxide PMD (premetal dielectric) deposition
	(d) Contact opening and metallization	Metal deposition, photolithography pattern and metal etch, then silicon oxide passivation and pad opening by photolithography and oxide etch
	(e) Ring structure pattern	Photolithography, silicon oxide etch, and 10 μm DRIE to form the ring structure at front
	(f) Front and back side release	A 5 μm anisotropic and 5 μm isotropic DRIE process for front side release and back side DRIE up to BOX layer is carried out for final release
 Silicon (substrate)	 Silicon (device layer)	 Photoresist
 SiO ₂ (BOX layer)	 SiO ₂ (PECVD)	 Aluminum

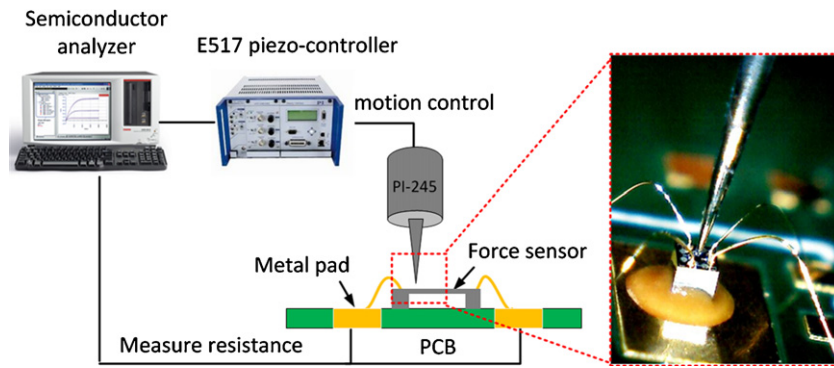


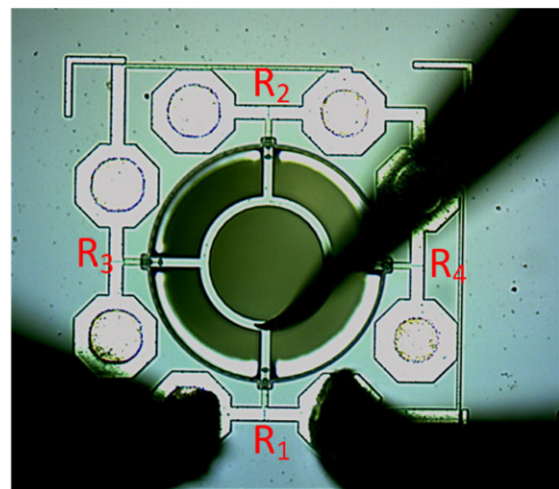
Figure 7. Schematic diagram of the experimental setup for the ring-shaped force sensor characterization. The inset is the enlarged view of the loading probe on top of the sensor.

by an oxide dry etching process to open the silicon area for isotropic plasma etch release. The oxide on the floor area was etched out while the sidewall oxide remained. Then, a $5\ \mu\text{m}$ anisotropic DRIE process followed by $5\ \mu\text{m}$ isotropic plasma etching (using a DRIE etcher) was processed to release the cantilever ring structure at the front. Then grinding and polishing were carried out at the wafer backside before the final back DRIE releasing process. The force sensor structure was finally released by using a backside DRIE process up to the BOX layer as shown in table 3(f). SEM images of the fabricated SiNW and the ring-shaped force sensor with four embedded SiNW piezoresistors are shown in figure 6.

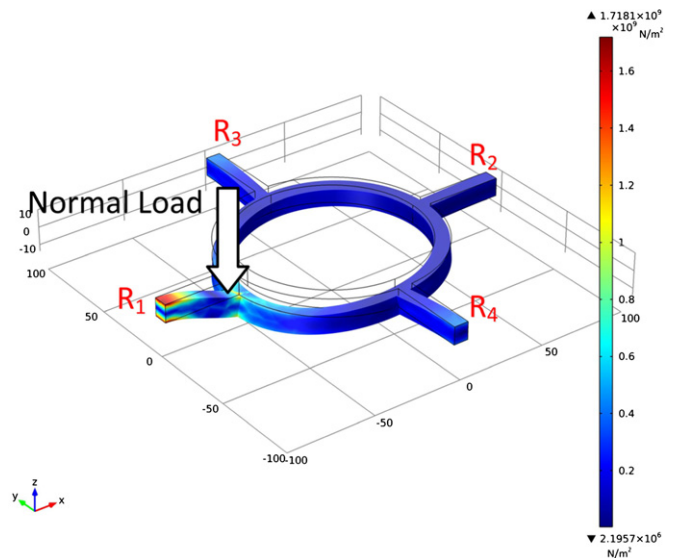
4. Device characterization and experimental results

4.1. Experimental setup

In order to calibrate and evaluate the functionality of the fabricated SiNW force sensor, characterization experiments have been conducted and the simulation results of characterization were used to verify experimental measurements. A schematic diagram of the experimental setup is shown in figure 7. The characterization system consists of a probe station with a microscope for visual control, a piezoactuator (PI-245) connected to a piezo motion controller (E517) for displacement loading control, and a Keithley 4200-SCS semiconductor analyzer to obtain the experimental data and, meanwhile, to control the piezo-controller. As demonstrated in figure 7, the sensor that wire bonded on a PCB board was fixed on the probe station through vacuum suction. The resistance of the SiNW was measured through the pads on the PCB and recorded by a semiconductor analyzer. Displacement loadings were applied through a piezoactuator (PI-245), which was controlled by the piezo-controller (E517). The resolution of the piezo-controller is 1.6 nm with a displacement range of 0–80 μm , which allows precise control of the step displacement. As shown in figure 8(a), displacement loading with various step sizes was applied through a probe needle at the end of one cantilever beam. The needle was firmly fixed in the probe holder, which was connected to the motion controller. The displacement of the structure was obtained by recording the displacement of the probe needle. To reduce the measurement uncertainty, we have considered the following conditions during the experiment.



(a)



(b)

Figure 8. Demonstration of the probe loading at the end of one cantilever under the view of a microscope (a) and simulation (b), where R_1 , R_2 , R_3 , and R_4 represent the resistance of SiNW resistors embedded at the anchor of each cantilever. The color bar in (b) represents the stress of the sensor in response to the prescribed displacement applied in the z -direction.

- Using a probe needle with large stiffness, which can attach firmly to the probe holder.

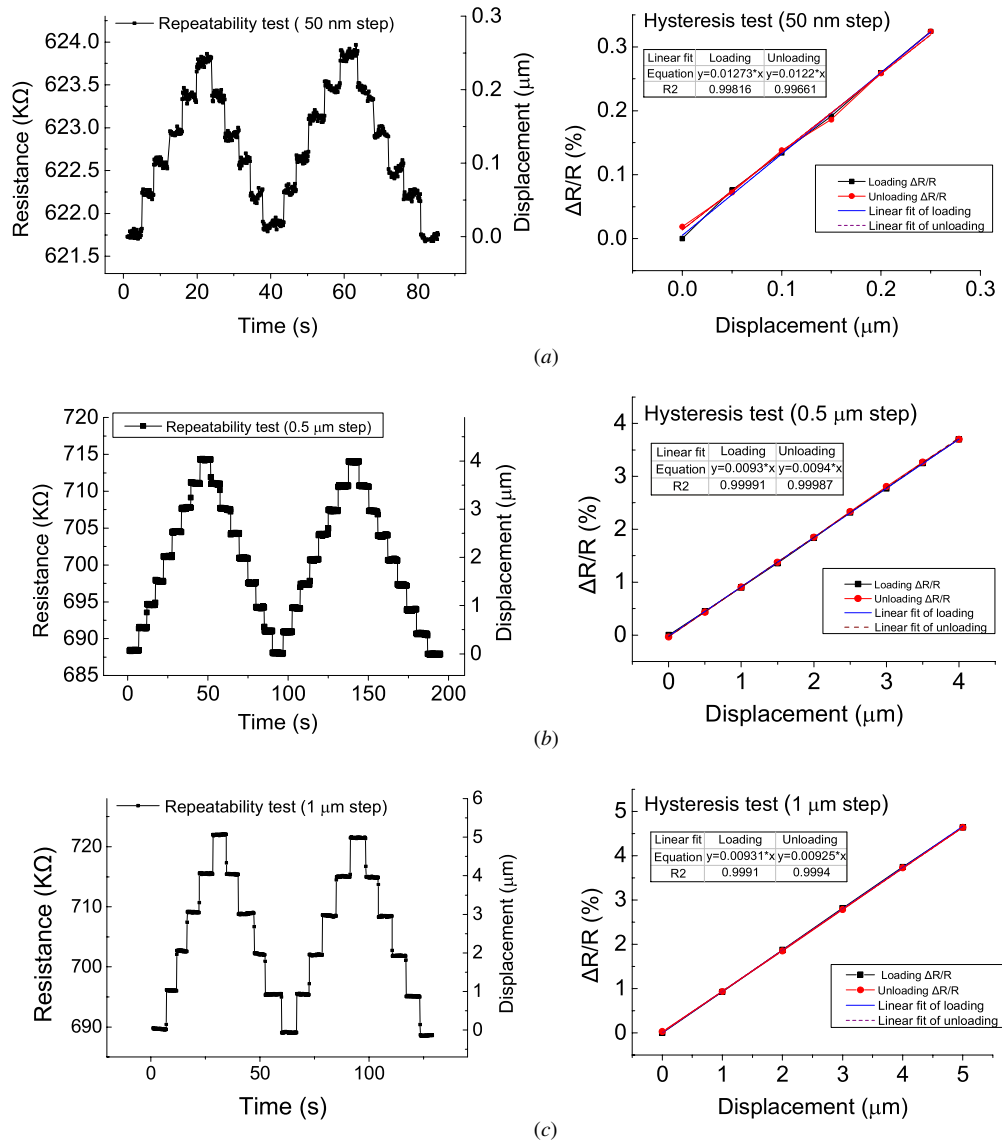


Figure 9. Repeatability and hysteresis tests for one SiNW piezoresistor on the sensor with displacement step size of: (a) 50 nm, (b) 0.5 μm, and (c) 1 μm, respectively. The linear fitting equations and adjacent R^2 values are shown in the right figures for the loading and unloading phases of the hysteresis cycle. Nanoscale displacement detection in a 50 nm step size with high repeatability is shown in (a). High linearity (99.9%) and no obvious hysteresis are demonstrated.

- Using a probe with a relatively large tip diameter.
- Decreasing the approaching speed of the needle to increase the contact stability.

A tungsten needle with a tip diameter of 3.5 μm was chosen as the loading probe for the measurement. The loading speed was considerably controlled to avoid the needle slipping during contact.

4.2. Characterization results

The repeatability and hysteresis test results for one SiNW piezoresistor are plotted in figure 9 with different displacement step sizes of (a) 50 nm, (b) 0.5 μm, and (c) 1 μm, respectively. In each case, the normal displacement was applied with an increasing step of (a) 50 nm, (b) 0.5 μm and (c) 1 μm and then decreased back to zero with the same step size along the z-direction. The loading cycle was repeated twice for each case.

Figure 9 (left) plots the resistance changes with respect to time. Linear fitting equations and adjacent R^2 values were calculated for the loading and unloading phases to obtain the hysteresis cycle shown in figure 9 (right). In figure 9(a), the SiNW ring-shaped force sensor showed nanoscale displacement detection in a 50 nm step size with high repeatability. From figure 9(a) (right), the end point of unloading cycle was not exactly zero. The error may be caused by resistance drift due to temperature as there was no temperature control implemented for the setup. From the repeatability and hysteresis test results, the sensor demonstrated high repeatability, high linearity (>99.9%) and no obvious hysteresis was observed as the two slopes of loading and unloading were almost coincident with each other, as shown in figure 9 (right). In addition, the resulting sensitivity of $S_{Dz} = 13.4 \times 10^{-3} \mu\text{m}^{-1}$ was obtained in the z-direction. From the noise level of the output resistance value, the displacement detection resolution of the force sensor

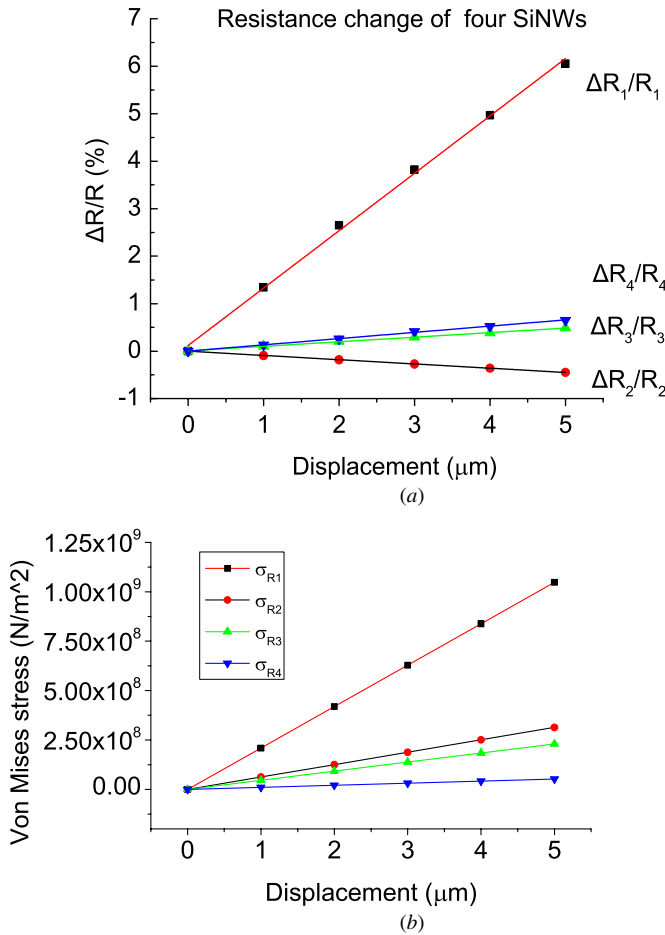


Figure 10. Experimental and simulation results: (a) experimental results of four SiNW piezoresistance change when load applied near R_1 , (b) simulation results of von Mises stress at four SiNW piezoresistors.

was determined to be 20.7 nm at a sampling rate of 8 Hz. To compare this work with other recently reported force sensor designs, the sensitivity and linearity of the ring-shaped sensor are summarized in table 1 with other recently reported piezoresistive tri-axial force sensors. As shown in columns five and six of table 1, comparing with the other recently reported force sensor designs using bulk implanted piezoresistors as sensing elements, the linearity and sensitivity of the SiNW-based force sensor have been improved.

The resistance change ratio of four SiNW piezoresistors with respect to displacement is plotted in figure 10(a). Normal loading was applied on piezoresistor R_1 , as demonstrated in figure 8(a). Obtained experimental results on $\Delta R/R$ versus normal displacement in figure 10(a) showed qualitative agreement with the stress–strain simulation of the ring-shaped force sensor as shown in figure 10(b). Ideally, when normal loading is applied, four piezoresistors under tensile stress should have the same signs of strain as shown in figure 10(b). However, a negative value of resistance change was observed for $\Delta R_2/R_2$ in figure 10(a), which means R_2 was under compressive stress during the loading cycle. This was caused mainly by an error in vertical loading on the sensor, where the angle between the loading probe and the sensor was not ideally 90° .

The force sensitivity of the device can be obtained from the displacement sensitivity characterization based on the stiffness of the beams. Each of the four identical cantilevers can be modeled as a fix-guided suspended beam, where one end is fixed to the support silicon and the other end is guide-fixed to the silicon ring. A vertical loading force F_z is applied at the guided end of the suspended beam. The relationship between the applied force and the resultant bending of the cantilever follows Hook’s law

$$F_z = K_e \Delta x, \quad (4)$$

where F_z is the loading force, K_e is the spring stiffness of the suspended beam, and Δx is the displacement of silicon ring.

The stiffness of each guided-beam with respect to normal loading force is given by

$$k_e = \frac{Ewt^3}{L^3} = 18.25 \times 10^3 \text{N/m}, \quad (5)$$

where E is the Young’s modulus, L , w , and t are the length, width, and thickness of the rectangular beam, respectively. Thus, with the known normal displacement sensitivity S_{Dz} of loading displacement D_z , the change in resistance per input force in the normal direction can be expressed with respect to the obtained resistance change by following:

$$S_{Fz} = \frac{S_{Dz}}{k_e} = \frac{\Delta R/R}{F_z} = 0.734 \text{N}^{-1}. \quad (6)$$

By applying equation (6) to the characterization results in figure 10(a), the normal displacement sensitivity of $13.4 \times 10^{-3} \mu\text{m}^{-1}$ yields a normal force sensitivity of 0.734N^{-1} .

Future characterization will be performed with a cylindrical mesa passing through the ring of the sensor acting as the guidewire. The mesa acts as the shear force transferring element in order to acquire the three components of the loading force, thus completing characterization of the sensor.

5. Conclusion

A ring-shaped tri-axial force sensor has been developed to be used on a guidewire in catheterization applications. The sensor has been designed with a ring structure for simple and smart integration on the distal tip of a guidewire. The mechanical behavior of the ring sensor with an integrated steel guidewire was simulated with FEM analysis. SiNWs with a length of $6 \mu\text{m}$ and a cross section of $90 \text{nm} \times 90 \text{nm}$ have been successfully fabricated by using the top-down approach on a SOI wafer. The device functionality has been verified by repeatability and hysteresis tests with different displacement step sizes including 50 nm, $0.5 \mu\text{m}$ and $1 \mu\text{m}$. The sensor showed high repeatability, high linearity ($>99.9\%$), and negligible hysteresis with a resistance change of 1.34 percent per micron displacement in the z -direction. In addition, the sensor shows nanoscale displacement detection in a 50 nm step size with high repeatability.

Acknowledgments

This work was supported by grants from A*STAR, SERC under grant no 0921480070 and 112 177 0039, and MOE

AcRF Tier 1 under grant no RG93/13 and RG35/10. This work was also supported by the Radiation Technology R&D program through the National Research Foundation of Korea funded by the Ministry of Science, ICT & Future Planning (NRF-2013M2A2A9043274). The authors would like to thank National University Hospital (NUH), Singapore for the scientific and technical consultation to the project. Beibei Han would like to thank the PhD research scholarship received from School of Mechanical and Aerospace Engineering of Nanyang Technological University.

References

- [1] Mueller R L and Sanborn T A 1995 The history of interventional cardiology: cardiac catheterization, angioplasty, and related interventions *Am. Heart J.* **129** 146–72
- [2] Guthart G S and Salisbury J K Jr 2000 The intuitive™ telesurgery system: overview and application *Proc. IEEE: Int. Conf. on Robot. and Automat. (ICRA, 2000)* pp 618–21
- [3] Isner J M, Kishel J, Kent K M, Ronan J A, Ross A M and Roberts W C 1981 Accuracy of angiographic determination of left main coronary arterial narrowing—angiographic-histologic correlative analysis in 28 patients *Circulation* **63** 1056–64
- [4] Razavi R et al 2003 Cardiac catheterisation guided by MRI in children and adults with congenital heart disease *Lancet* **362** 1877–82
- [5] Nissen S E and Yock P 2001 Intravascular ultrasound—novel pathophysiological insights and current clinical applications *Circulation* **103** 604–16
- [6] Haga Y, Fujita M, Nakamura K, Kim C J and Esashi M 2003 Batch fabrication of intravascular forward-looking ultrasonic probe *Sensors Actuators A* **104** 40–3
- [7] Okumura Y, Johnson S B, Bunch T J, Henz B D, O'Brien C J and Packer D L 2008 A systematical analysis of *in vivo* contact forces on virtual catheter tip/tissue surface contact during cardiac mapping and intervention *J. Cardiovasc. Electrophysiol.* **19** 632–40
- [8] Yokoyama K et al 2008 Novel contact force sensor incorporated in irrigated radiofrequency ablation catheter predicts lesion size and incidence of steam pop and thrombus *Circ.-Arrhythmia Electrophysiol.* **1** 354–62
- [9] Thiagalingam A, D'Avila A, Foley L, Guerrero J L, Lambert H, Leo G, Ruskin J N and Reddy V Y 2010 Importance of catheter contact force during irrigated radiofrequency ablation: evaluation in a porcine *ex vivo* model using a force-sensing catheter *J. Cardiovasc. Electrophysiol.* **21** 806–11
- [10] Haga Y and Esashi M 2004 Biomedical microsystems for minimally invasive diagnosis and treatment *Proc. IEEE* **92** 98–114
- [11] Polygerinos P, Zbyszewski D, Schaeffter T, Razavi R, Seneviratne L D and Althoefer K 2010 MRI-compatible fiber-optic force sensors for catheterization procedures *IEEE Sens. J.* **10** 1598–608
- [12] Tiwana M I, Redmond S J and Lovell N H 2012 A review of tactile sensing technologies with applications in biomedical engineering *Sensors Actuators A* **179** 17–31
- [13] Esashi M, Komatsu H, Matsuo T, Takahashi M, Takishima T, Imabayashi K and Ozawa H 1982 Fabrication of catheter-tip and sidewall miniature pressure sensors *IEEE Trans. Electron Devices* **29** 57–63
- [14] Kalvesten E, Smith L, Tenerz L and Stemme G 1998 The first surface micromachined pressure sensor for cardiovascular pressure measurements *IEEE MEMS (1998)* pp 574–9
- [15] Tanimoto M, Arai F, Fukuda T, Iwata H, Itoigawa K, Gotoh Y, Hashimoto M and Negoro M 1998 Micro force sensor for intravascular neurosurgery and *in vivo* experiment *Proc. MEMS (1998)* pp 504–9
- [16] Meiß T, Kern T A, Sindlinger S and Werthschützky R 2009 HapCath: highly miniaturized piezoresistive force sensors for interior palpation of vessels during angioplasty *IFMBE Proceedings: World Congress on Medical Physics and Biomedical Engineering (Berlin: Springer)* pp 228–31
- [17] Kalantari M, Ramezanifard M, Ahmadi R, Dargahi J and Kovacs J 2011 A piezoresistive tactile sensor for tissue characterization during catheter-based cardiac surgery *Int. J. Med. Robot.* **7** 431–40
- [18] Park W T, Kotlanka R K, Lou L, Hamidullah M and Lee C 2012 MEMS tri-axial force sensor with an integrated mechanical stopper for guidewire applications *Microsyst. Technol.* **19** 1005–15
- [19] Han B, Yoon Y-J, Hamidullah M, Lin A T-H and Park W-T 2013 Silicon nanowire based ring shape force sensor for sensorized guidewires *17th Int. Conf. on Solid-State Sensors, Actuators and Microsystems (Barcelona, Spain)* pp 718–21
- [20] Hammarström O, Benkowski P, Malmborg P V and Tenerz L 2002 Sensor and guide wire assembly Radi Medical Systems AB *US Patent No.* 6336906
- [21] Chu Z, Sarro P M and Middelhoek S 1996 Silicon three-axial tactile sensor *Sensors Actuators A* **54** 505–10
- [22] Kane B J, Cutkosky M R and Kovacs G T A 2000 A traction stress sensor array for use in high-resolution robotic tactile imaging *J. Microelectromech. Syst.* **9** 425–34
- [23] Wang L and Beebe D J 2000 A silicon-based shear force sensor: development and characterization *Sensors Actuators A* **84** 33–44
- [24] Bütefisch S, Büttgenbach S, Kleine-Besten T and Brand U 2001 Micromechanical three-axial tactile force sensor for micromaterial characterisation *Microsyst. Technol.* **7** 171–4
- [25] Beccai L, Roccella S, Arena A, Valvo F, Valdastrì P, Menciassi A, Carrozza M C and Dario P 2005 Design and fabrication of a hybrid silicon three-axial force sensor for biomechanical applications *Sensors Actuators A* **120** 370–82
- [26] Vázsonyi É, Ádám M, Dücső C, Vízváry Z, Tóth A L and Bársony I 2005 Three-dimensional force sensor by novel alkaline etching technique *Sensors Actuators A* **123–124** 620–6
- [27] Vasarhelyi G, Adam M, Vazsonyi E, Vizvary Z, Kis A, Barsony I and Ducso C 2006 Characterization of an integrable single-crystalline 3D tactile sensor *IEEE Sens. J.* **6** 928–34
- [28] Hu Y, Katragadda R B, Tu H, Zheng Q, Li Y and Xu Y 2010 Bioinspired 3D tactile sensor for minimally invasive surgery *J. Microelectromech. Syst.* **19** 1400–8
- [29] Zhang Y 2010 Sensitivity enhancement of a micro-scale biomimetic tactile sensor with epidermal ridges *J. Micromech. Microeng.* **20** 085012
- [30] He R R and Yang P D 2006 Giant piezoresistance effect in silicon nanowires *Nature Nanotechnol.* **1** 42–6
- [31] Rowe A C H 2008 Silicon nanowires feel the pinch *Nature Nanotechnol.* **3** 311–2
- [32] Singh P, Park W-T, Miao J, Shao L, Krishna Kotlanka R and Kwong D-L 2012 Tunable piezoresistance and noise in gate-all-around nanowire field-effect-transistor *Appl. Phys. Lett.* **100** 063106
- [33] Barlian A A, Park W T, Mallon J R, Rastegar A J and Pruitt B L 2009 Review: semiconductor piezoresistance for microsystems *Proc. IEEE* **97** 513–52
- [34] Toriyama T, Tanimoto Y and Sugiyama S 2002 Single crystal silicon nano-wire piezoresistors for mechanical sensors *J. Microelectromech. Syst.* **11** 605–11

- [35] Paska Y and Haick H 2012 Interactive effect of hysteresis and surface chemistry on gated silicon nanowire gas sensors *ACS Appl. Mater. Interfaces* **4** 2604–17
- [36] Lou L *et al* 2010 Sensorized guidewires with MEMS tri-axial force sensor for minimally invasive surgical applications *Annu. Int. Conf. of the IEEE, Eng. in Med. and Bio. Soc. (EMBC, 2010)* pp 6461–4
- [37] Singh P, Miao J, Park W-T and Kwong D-L 2011 Gate-bias-controlled sensitivity and SNR enhancement in a nanowire FET pressure sensor *J. Micromech. Microeng.* **21** 105007
- [38] Lou L, Zhang S, Park W-T, Tsai J M, Kwong D-L and Lee C 2012 Optimization of NEMS pressure sensors with a multilayered diaphragm using silicon nanowires as piezoresistive sensing elements *J. Micromech. Microeng.* **22** 055012
- [39] Zhang S, Lou L and Lee C 2012 Piezoresistive silicon nanowire based nanoelectromechanical system cantilever air flow sensor *Appl. Phys. Lett.* **100** 023111
- [40] Zhang Y, Liu X Y, Ru C H, Zhang Y L, Dong L X and Sun Y 2011 Piezoresistivity characterization of synthetic silicon nanowires using a MEMS device *J. Microelectromech. Syst.* **20** 959–67
- [41] Singh N, Buddharaju K D, Manhas S K, Agarwal A, Rustagi S C, Lo G Q, Balasubramanian N and Kwong D-L 2008 Si, SiGe nanowire devices by top-down technology and their applications *IEEE Trans. Electron Devices* **55** 3107–18
- [42] Erglis A, Narbutė I, Sondore D, Grave A and Jegere S 2010 Tools & Techniques: coronary guidewires *Euro Interv.* **6** 1–8
- [43] ISO 1998 Sterile, single-use intravascular catheter introducers ISO 11070 www.iso.org/iso/iso_catalogue/catalogue_tc/catalogue_detail.htm?csnumber=19052
- [44] Simpson J B, Baim D S, Robert E W and Harrison D C 1982 A new catheter system for coronary angioplasty *Am. J. Cardiol.* **49** 1216–22
- [45] Chan K L, Tiew K-T, Astuti Lee A, Luo J, Ng S S Y and Je M 2010 A tactile sensor ASIC for a sensorized guidewire in minimally invasive surgical operations *IEEE Asian, Solid State Circuits Conf. (A-SSCC, 2010)* pp 1–4
- [46] Bassou E 1978 Fabrication of novel three-dimensional microstructures by the anisotropic etching of *IEEE Trans. Electron Devices* **25** 1178–85
- [47] Gere J M and Goodno B J 2009 *Mechanics of Materials* (Toronto, ON: Cengage Learning)
- [48] Hopcroft M A, Nix W D and Kenny T W 2010 What is the Young's modulus of silicon? *J. Microelectromech. Syst.* **19** 229–38
- [49] Madou M J 2002 *Fundamentals of Microfabrication: The Science of Miniaturization* 2nd edn (Boca Raton, FL: CRC Press)
- [50] Senturia S D 2001 *Microsystem Design* (Boston, MA: Kluwer Academic)